

Understanding Hip Fracture by QCT-Based Finite Element Modeling

Hossein Kheirollahi¹ · Yunhua Luo^{1,2}

Received: 28 October 2015 / Accepted: 8 June 2017 / Published online: 19 June 2017
© Taiwanese Society of Biomedical Engineering 2017

Abstract Hip fracture has become a common health problem among old people. Understanding hip fracture mechanics is the first step to effectively prevent hip fracture. The objective of this study was to investigate the combined effect of reversed stress/strain patterns in femur (during single-leg stance and sideways fall) and the inhomogeneous material properties of femur bone. We constructed 40 subject-specific femur finite element models from medical quantitative computed tomography and used them to identify high risk regions in the femur induced by the two loading configurations. The obtained results showed that compared to the single-leg stance, in the sideways fall the highest stress and strain occurred at different locations; and the tensile-compressive stress status was also completely reversed. Previous studies have found that a bone has different strength at different anatomic sites, and at the same site it has different compressive and tensile strength. Our study suggested that, in addition to the large magnitude of impact force induced in falling, the abnormal stress/strain patterns produced by the non-habitual loading condition in falling may be another external contributor to hip fracture.

Keywords Hip fracture · Single-leg stance · Sideways fall · Quantitative computed tomography (QCT) · Finite element model

1 Introduction

The femur is the longest bone in the human body. For the elderly, especially for those who have osteoporosis, the femur is prone to fracture during walking and falling. Incidence of hip fractures is continuously increasing and has become a common health problem for the elderly over the world. Hip fracture is associated with 20% chance of death, 25% chance of long term disability and less than 50% chance of full recovery [1]. The devastating sequelae of hip fracture have motivated us to develop biomechanical models to understand hip fracture mechanics, so that more effective prevention and protection measurements can be designed.

Hip fracture is dominantly determined by the stress and strain distributions in the femur, which are affected by a number of factors such as the subject's height, weight, femur size, and bone inhomogeneous material properties. All these factors are subject-dependent. Therefore, a subject-specific finite element model is necessary to accurately predict femur stresses and strains [2–6]. High stress and strain regions in the femur are the potential locations of crack initiation in hip fracture. Knowledge of high stress/strain regions in femur during normal walking and falling helps us to understand its mechanical behavior and failure mechanism. A number of image-based finite element models have been developed for studying hip fractures. They were mainly developed from dual-energy X-ray absorptiometry (DXA) or quantitative computed tomography (QCT). DXA-based FE models are inherently two-dimensional (2-D) and they are not able to faithfully represent bone geometry and material distribution. Therefore, three-dimensional QCT-based FE models were used in our studies of hip fracture.

QCT-based finite element models have been applied to predict potential fracture location, bone strength, fracture

✉ Yunhua Luo
Yunhua.Luo@umanitoba.ca

¹ Department of Mechanical Engineering, University of Manitoba, Winnipeg R3T 2N2, Canada

² Department of Biomedical Engineering, University of Manitoba, Winnipeg R3T 2N2, Canada

load, and stress/strain distribution [2–6]. The global maximum stress or strain has been used in evaluation of hip fracture risk, which may not be clinically helpful, as clinical observations have revealed that the majority of hip fractures often occurred at the narrowest femoral neck, the intertrochanteric, and the subtrochanteric cross-section [7]. Therefore, in our study, we focused on the above three critical regions to evaluate fracture risk.

2 Materials and Methods

In this section the procedure for constructing QCT-based FE models is described, which includes the acquisition of femur QCT scans, produce of femur geometric models, generation of finite element meshes, assignment of material properties, finite element analyses with ANSYS (Ansys, Inc., USA), and stress/strain extraction over the three critical regions of interest (ROI).

2.1 Femur QCT Scans

QCT scans were acquired of the entire femur using the CT portion of a Biograph 16 PET/CT system (Siemens Medical Solutions, Knoxville, TN). This CT system is equivalent to a Siemens Sensation 16. Images were acquired in spiral mode using a 120 kVp, 175 effective mAs technique with the CARE Dose4D option enabled. Data were reconstructed using 3 mm slice thickness and in-plane resolution of 0.5 pixel/mm with B40s kernel. The scanned QCT images were stored in the format of Digital Imaging and Communications in Medicine (DICOM). Each voxel in the QCT scan has an intensity (or grey scale) expressed as Hounsfield Unit (HU), which is correlated to bone density [8, 9]. Femur QCT images of 20 subjects (10 females and 10 males, both right and left femur, totally 40 femurs) were scanned at the Winnipeg Health Science Centre in an anonymous way under a human research ethics approval. The statistics of the subjects are provided in Table 1.

2.2 Femur Geometric Model and Finite Element Mesh

Geometrical models of the femurs were produced from the acquired QCT images using Mimics (Materialise, Leuven, Belgium). The QCT images (in DICOM format) of a

subject were imported to Mimics for segmentation (Fig. 1a) and a 3-D geometric model of the femur was constructed (Fig. 1b). With the 3-D geometric model, a FE mesh was generated using the 3-matic module in Mimics (Fig. 1c). The 4-node linear tetrahedral element SOLID72 in ANSYS was used in this study. To investigate model convergence, FE models with different maximum element edge lengths were created. For each FE model, the maximum von Mises stress at the narrowest femoral neck cross-section was calculated under the same loading and boundary conditions. The maximum element edge length that produced converged finite element solutions was obtained and used in all the rest FE simulations. A typical convergence curve of von-Mises stress is displayed in Fig. 2.

2.3 Assignment of Material Properties

Bone material properties were considered as inhomogeneous and isotropic in this study. The inhomogeneous isotropic mechanical properties of the bones are obtained from the CT data using a mathematical relationship between CT numbers and mechanical properties of bone. The following empirical equation was used to determine bone ash density (ρ_{ash}) from HU number [3, 10]:

$$\rho_{ash} = 0.04162 + 0.000854 HU \text{ (g/cm}^3\text{)} \quad (1)$$

Bone elasticity modulus and compressive yield stress are derived from bone ash density by [11],

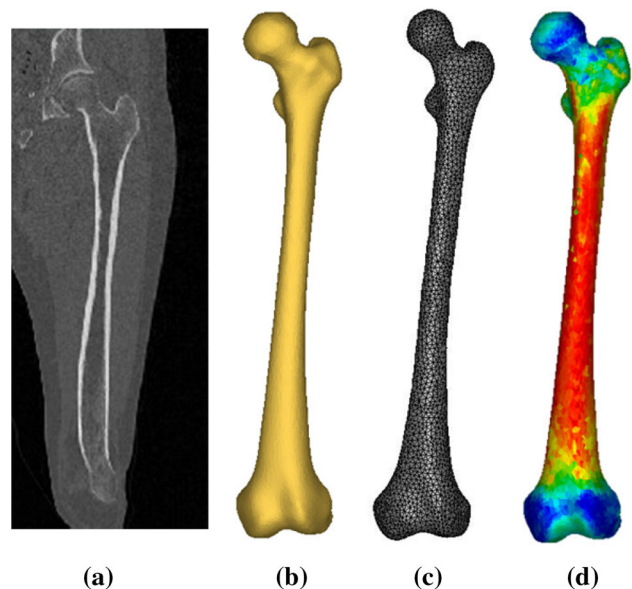


Fig. 1 Subject-specific QCT-based finite element model: **a** QCT scan of the subject's femur, **b** 3-D geometric model generated from the QCT scans, **c** 3-D finite element mesh, and **d** inhomogeneous material property (elasticity modulus)

Table 1 Statistical characteristics of subjects

Age (years)	62.6 ± 7.1
Height (cm)	156.9 ± 12.1
Weight (kg)	53.7 ± 6.9
BMI (kg/cm^2)	26.9 ± 5.2

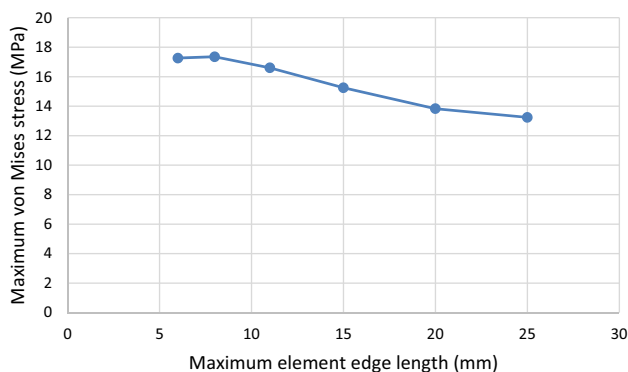


Fig. 2 Convergence of maximum von Mises stress with element size (femoral neck)

$$E = 10,500 \rho_{ash}^{2.29} \text{ (MPa)} \tag{2}$$

$$\sigma_Y = 116 \rho_{ash}^{2.03} \text{ (MPa)} \tag{3}$$

The tensile yield stress is considered as 80% of the compressive yield stress [12]. A constant Poisson’s ratio ($\nu = 0.4$) was considered [13, 14]. To assign material properties, elements were grouped into several discrete material bins using Mimics (Materialise, Leuven, Belgium), which were used to approximately represent the continuous distribution of the inhomogeneous bone mechanical properties. To determine the maximum number of material bins, convergence study was performed. Models with different material bins were created for the convergence study. For each FE model, the maximum von Mises stress at the smallest femoral neck cross-section was calculated under the same loading and boundary conditions. The minimum number of material bins that generated converged finite element solutions was obtained. Figure 1d shows the isotropic inhomogeneous distribution of bone elasticity modulus.

2.4 Finite Element Analysis Using ANSYS

The finite element model of the subject’s femur with the assigned material properties was output from Mimics, and then imported to ANSYS for finite element analysis. Loading and boundary conditions simulating the single-leg stance and the sideways fall were considered. To simulate the single-leg stance statue, 2.5 times of the patient’s body weight was applied as a distributed load on the femoral head [15] and the femur was fixed at the distal end [5, 13], see Fig. 3a,

$$F_{Stance} = 2.5w \text{ (N)}, \tag{4}$$

where w is the subject’s body weight in Newton (N). To simulate the sideways fall, the distal end of the femur and the femoral head were constrained [6, 16] (see Fig. 3b). The impact force induced in the sideways fall and applied on the greater trochanter (Fig. 3b) was estimated by [15, 17]:

$$F_{Impact} = 8.25w \left(\frac{h}{170} \right)^{\frac{1}{2}} \text{ (N)}, \tag{5}$$

where h is the height of the subject in centimeter (cm). The above loading and boundary conditions were applied to a group of nodes using ANSYS Parametric Design Language (APDL) codes. After importing the QCT-based FE model with the loading and boundary conditions, finite element analysis was performed and finite element solutions were obtained. In all the analyses, stresses and strains were obtained for the subjects.

2.5 The Three Critical Cross-Sections on the Femur

Hip fractures usually occur at one of the three locations, i.e., the femoral neck, the intertrochanteric, and the subtrochanteric as shown in Fig. 4. According to clinical observations, 49% of hip fractures are intertrochanteric, 37% are at femoral neck, and 14% are subtrochanteric [7]. Therefore, the narrowest femoral neck cross-section (SFN CS), the intertrochanteric cross-section (IntT CS), and the subtrochanteric cross-section (SubT CS) are the three most critical cross-sections where a fracture is likely to occur. In our study, the three critical cross-sections were determined in the following steps. The femoral neck-shaft angle was first determined. The neck-shaft angle is the angle between the femoral neck axis and the femoral shaft axis. This angle traditionally is measured on radiography images or 2-D images projected from CT/MRI data. The method uses an over-simplified femur geometry and thus may introduce large errors, especially in the selection of a proper measurement plane [18–20]. In our study, the neck-shaft angle was measured using a 3-D measurement technique based on a set of fitting functions. The shapes of particular parts of the femur were approximated using geometric entities such as circle, cylinder, and sphere, which are able to better fit to the actual geometry, and the geometrical relationships among these entities were used to estimate the neck-shaft angle.

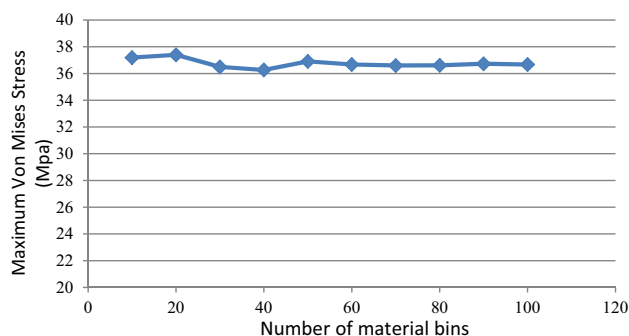


Fig. 3 Convergence of von Mises stress at femoral neck with material bins

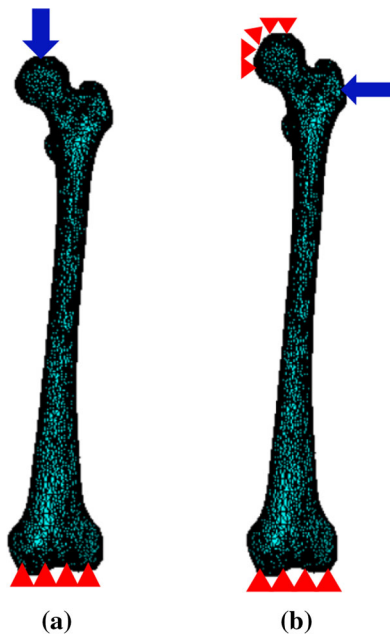


Fig. 4 Loading and constraint conditions during **a** single-leg stance and **b** sideways fall

First, a sphere was fitted to the femoral head, and the center of femoral head was determined. Then, the femoral neck axis and the femoral shaft axis were identified by applying the “fit ruled surface direction” function on the femoral neck and shaft. All fitting functions were applied using the 3-matic module in Mimics. The neck-shaft angle was measured by the 3-matic module in Mimics (Fig. 5). With the femoral neck shaft-angle, the intertrochanteric cross-section and the narrowest femoral neck cross-section were found using in-house computer codes [21, 22]. The narrowest femoral neck cross-section was chosen as the cross-section of the smallest area at femoral neck, and the intertrochanteric cross-section was chosen as the cross-section that has the largest area in the intertrochanteric region [23]. By using ANSYS APDL codes, a plane perpendicular to the femoral neck axis was determined, and the area of the cross-sections was calculated (Fig. 6). Planes with the smallest and the largest areas were chosen, respectively, as the smallest femoral neck cross-section and the intertrochanteric cross-section. The subtrochanteric cross-section was located at 5 cm below the lesser trochanter [24] (Fig. 6).

3 Results and Discussion

3.1 Convergence Study

The convergence of finite element solutions is usually achieved by refining the finite element mesh. The maximum

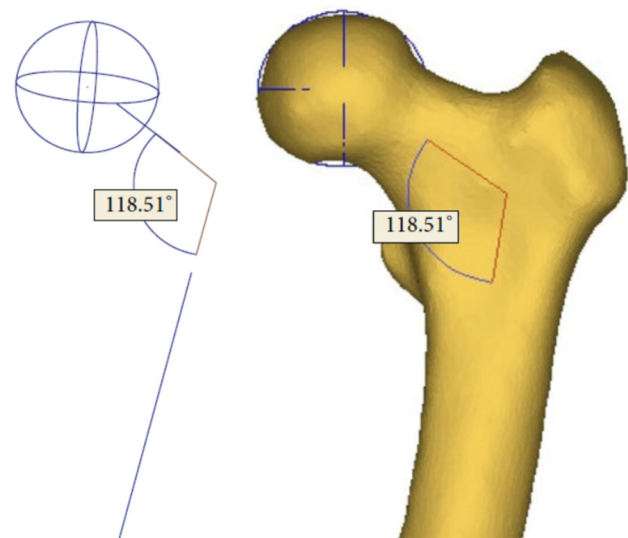


Fig. 5 Neck-shaft angle measured by the fitting functions in the 3-matic module of Mimics

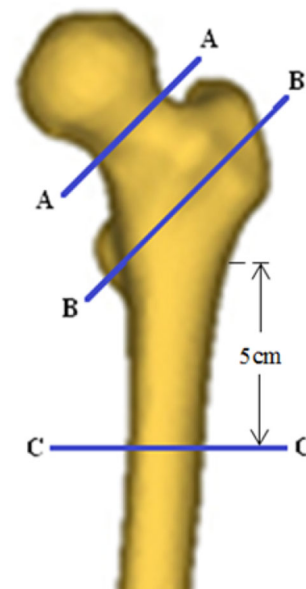


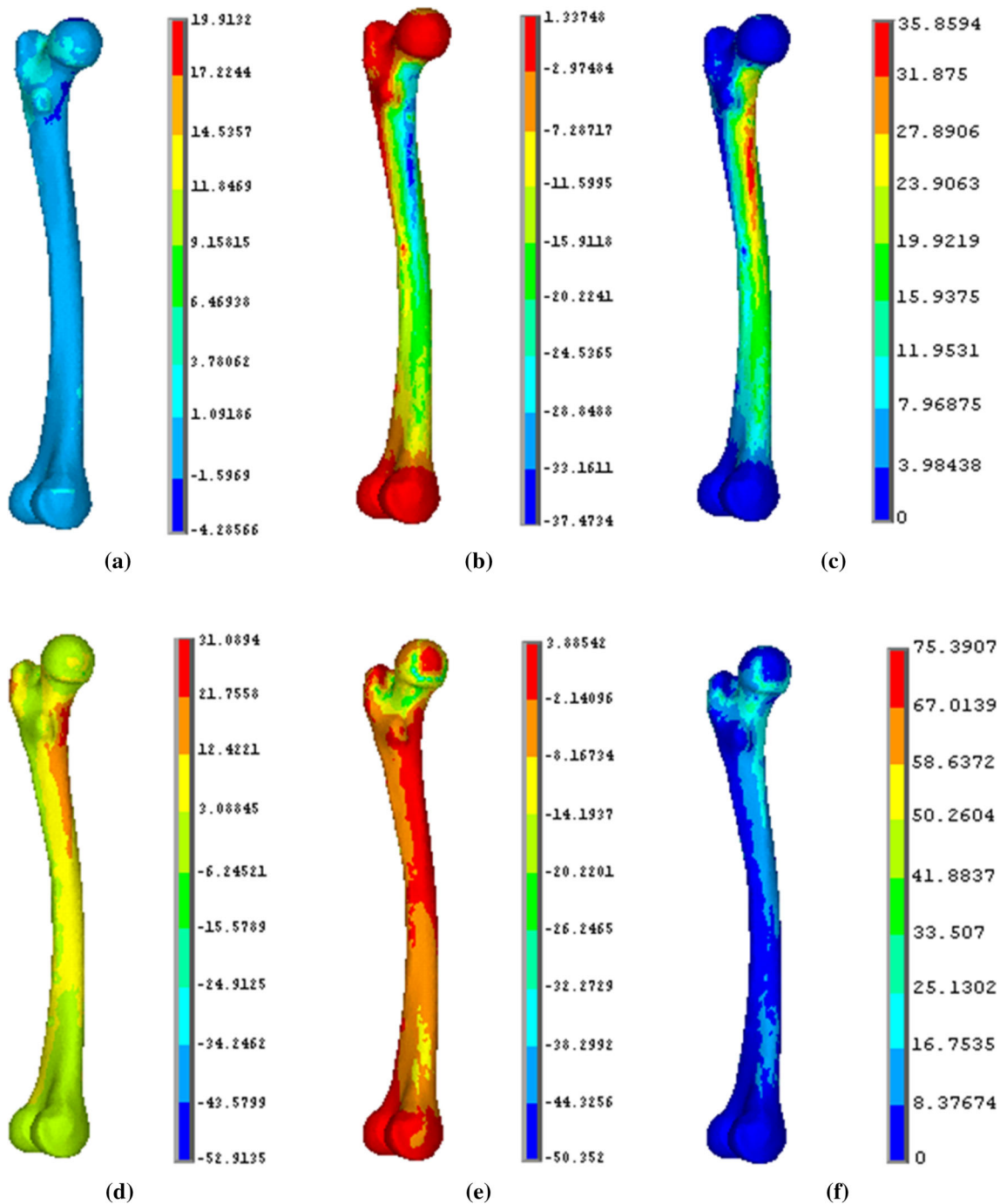
Fig. 6 The three critical cross-sections of femur: the smallest femoral neck cross-section (A–A), the intertrochanteric cross-section (B–B), and the subtrochanteric cross-section (C–C)

von Mises stress at the narrowest femoral neck was monitored to judge whether a convergence had been achieved, or not. The typical convergence curve in Fig. 2 shows that the maximum von Mises stress at the narrowest femoral neck converged with the maximum element edge length smaller than 8 mm. Therefore, in the construction of all femur FE models, the maximum element edge length was set to 8 mm.

To study the convergence in the assigned inhomogeneous material properties, a number of femur FE models with different number of material bins were created. The

Table 2 Average maximum von Mises stress (MPa) at the smallest femoral neck cross-section (SFN CS), the intertrochanteric cross-section (IntT CS), and the subtrochanteric cross-section (SubT CS) for 40 femurs in the single-leg stance and sideways fall

	Single-leg stance			Sideways fall		
	SFN CS	IntT CS	SubT CS	SFN CS	IntT CS	SubT CS
Range	28.5–43.6	26.3–59.7	33.4–97.7	257.2–159.7	31.8–79.3	19.3–42.5
Average	30.3	42.5	62.7	78.4	59.5	41.3

**Fig. 7** Stress distribution (MPa) during the single-leg stance: **a** tensile stress, **b** compressive stress, **c** von Mises stress; and in the sideways fall: **d** tensile stress, **e** compressive stress, **f** von Mises stress

loading and boundary conditions were kept the same in FE models. For each FE model, the maximum von Mises stress at the narrowest femoral neck was monitored. The representative convergence result in Fig. 3 shows that a convergence was achieved with the number of material bins larger than 50. Therefore, 50 material bins were used in all the femur FE models.

3.2 Change in the Location of the Maximum Stresses and Strains

The average maximum von Mises stresses at the three critical cross-sections (i.e. the smallest femoral neck, the intertrochanteric and the subtrochanteric cross-sections) for the 40 femurs are provided in Table 2. The distributions of tensile, compressive and von Mises stress over the femur in a typical case are displayed in Fig. 7. The average maximum effective strains at the three critical cross-sections are listed in Table 3.

By comparing the stress patterns in the single-leg stance configuration (Fig. 7a–c) with those in the sideways fall (Fig. 7d–f), it can be seen that the locations of maximum tensile, compressive and von Mises stresses are completely different. For example, Fig. 7b shows that in the single-leg stance configuration, the proximal medial side of the femur had the highest compressive stress; however, in the sideways fall, the same region had the highest tensile stress. From Table 2, in the single-leg stance configuration, the subtrochanteric cross-section had the highest von Mises stress, followed by the intertrochanteric and then the smallest femoral neck cross-section. However, in the sideways fall the smallest femoral neck cross-section had the highest (and also the largest increase in) von Mises stress, followed by the

intertrochanteric and the subtrochanteric cross-sections. The stress at the subtrochanteric cross-section was even smaller than that in the single-leg stance configuration.

Based on the Wolff’s law [25, 26], a bone in a healthy human body will adapt to withstand the long-term loading. If the loading on a particular bone increases, the bone will remodel itself over the time to become stronger to resist that sort of loading. If the law is applied to a single bone, it can be interpreted that the portion of the bone that sustains larger stresses over the time will have higher bone density and larger ultimate (or yield) stress than the other portions [27, 28]. The single-leg stance configuration is apparently the habitual loading condition for the human body, which thus governs the density distribution and local strength of the femur. Based on the Wolff’s law and the stress level in Table 2, the subtrochanteric cross-section is expected to have the highest bone density, and the narrowest femoral neck cross-section should have the lowest BMD. By using QCT Pro (Mindways, Austin, USA), we obtained the average volumetric BMD of the subjects over the three cross-sections. The BMD at the smallest femoral neck cross-section is $508.9 \pm 71.8 \text{ mg/cm}^3$, the intertrochanteric cross-section $571.2 \pm 54.1 \text{ mg/cm}^3$, and the subtrochanteric cross-section $910.0 \pm 70.7 \text{ mg/cm}^3$. Based on Eqs. (2) and (3), the subtrochanteric cross-section has the highest elasticity modulus and yield stress; and the narrowest femoral neck cross-section and the intertrochanteric cross-section have lower strength. In the sideways fall, the impact force is not a habitual loading for the human body, and the stress distributions produced by the impact force are abnormal. Tables 2 and 3 show that the weakest femoral neck had the highest stress and strain level in the sideways fall.

Table 3 Average maximum effective strain ($\times 10^{-6}$) at the smallest femoral neck cross-section (SFN CS), the intertrochanteric cross-section (IntT CS), and the subtrochanteric cross-section (SubT CS) for 40 femurs during the single-leg stance and sideways fall

	Single-leg stance			Sideways fall		
	SFN CS	IntT CS	SubT CS	SFN CS	IntT CS	SubT CS
Range	626.2–852.9	432.1–746.3	726.4–932.2	882.5–1644.2	577.3–873.9	450.4–622.3
Average	538.8	598.3	817.9	1198.8	677.4	558.3

Table 4 Average maximum tensile and compressive stress for 40 femurs in the femoral neck during the single-leg stance and sideways fall

	Single-leg stance		Sideways fall	
	Maximum tensile stress (MPa)	Maximum compressive stress (MPa)	Maximum tensile stress (MPa)	Maximum compressive stress (MPa)
Location	28.6	38.2	102.6	79.8
	Superior femoral neck	Inferior femoral neck	Inferior femoral neck	Superior femoral neck

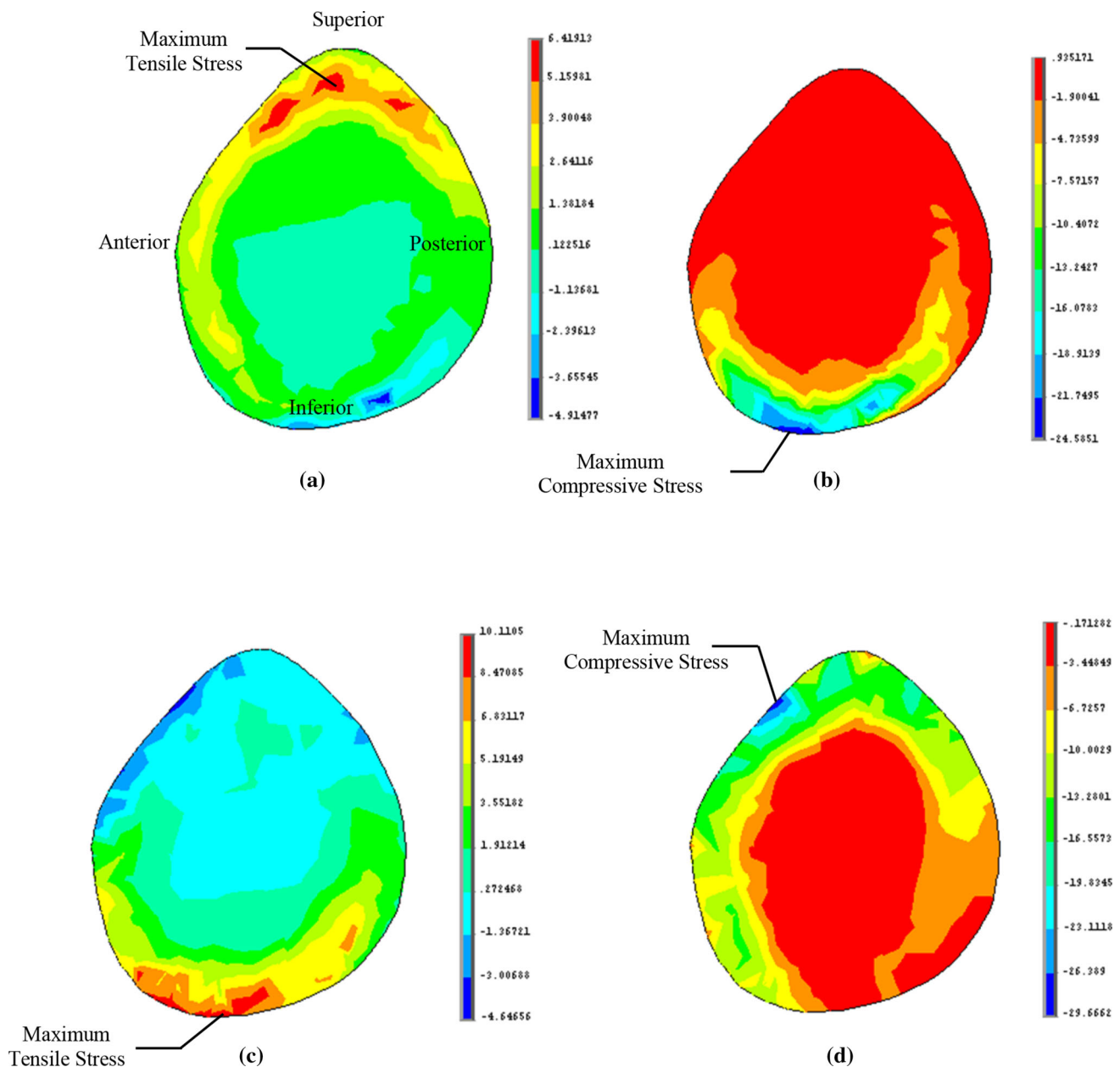


Fig. 8 Stress distribution (MPa) at the smallest femoral neck cross-section during the single-leg stance: **a** tensile stress, **b** compressive stress; and in the sideways fall: **c** tensile stress, **d** compressive stress

3.3 Reverse of Tensile-Compressive Stress Status over the Smallest Femoral Neck Cross-Section

The average tensile and compressive stresses for the 40 femurs and their corresponding locations over the narrowest femoral neck cross-section during the single-leg stance and sideways fall are provided in Table 4. The distributions of tensile and compressive stresses over the narrowest femoral neck cross-section in a typical case are displayed in Fig. 8. The results showed that the superior side of femoral neck experienced high tensile stress in the

single-leg stance, but had high compressive stress in the sideways fall; the inferior side sustained high compressive stress in the single-leg stance configuration, but received high tensile stress in the sideways fall. Therefore, the compressive-tensile stress status over the femoral neck in the sideways fall was completely reversed.

Cortical and cancellous bones have different strengths in tension and compression. Cancellous bone has significantly higher strength in tensile testing [2]. While cortical bone usually has considerably higher compressive strength. The average ratio of cortical bone tensile to compressive yield

strength has been reported as 0.56 by Reilly et al. [14] and as 0.62 by Bayraktar et al. [2]. The superior side of femoral neck is dominated by cancellous bones that are more favorable to sustain tensile stresses, but large compressive stresses occurred in this region during the sideways fall. In addition, the cortical bone at the superior side of femoral neck is thin, especially for osteoporosis patients. Under the action of large compressive stress, the thin cortical shell at the superior side is likely to buckle. After the buckling, the femoral neck will have much smaller bending moment of inertia and cross-section stiffness, thus, the failure will propagate to the inferior side. The experiment studies conducted by Bakker et al. [29] using cadaveric femora showed that most femur fractures indeed started from the superior side of the femoral neck.

4 Conclusion

In this paper, the stress and strain patterns in the proximal femur during the single-leg stance and sideways fall were studied by subject-specific finite element models constructed from the subjects' femur QCT scans. The obtained results showed that compared to the habitual physiological loading condition (i.e. the single-leg stance), in the sideways fall the locations of maximum stress and strain in the femur were changed in such a way that the weakest part of the femur (the femoral neck) had to withstand the largest stress/strain induced by the impact force; what made the situation even worse is that the compressive-tensile stress status in the femur, especially at the femoral neck, was totally reversed from the habitual loading condition. The impact force induced in the sideways fall usually has a larger magnitude compared with the habitual physiological loading. In the sideways fall, the shift in the location of maximum stress/strain and the reverse of tensile-compressive stress status created the most unfavorable situation for the femur to withstand the impact force.

Acknowledgements The reported research was supported by the Natural Sciences and Engineering Research Council (NSERC) and Research Manitoba of Canada, which are gratefully acknowledged.

Compliance with ethical standards

Conflict of interest There is no conflict of interest involved in the reported study or in the published results.

Ethical approval The QCT images used in this study were acquired from Health Science Centre located at Winnipeg under an Ethical Approval issued by the Research Ethics Board (REB) of the University of Manitoba.

References

1. Resnick, N. M., & Greenspan, S. L. (1989). 'Senile' osteoporosis reconsidered. *JAMA*, *261*, 1025–1029.
2. Keyak, J. H., Rossi, S. A., Jones, K. A., Les, C. M., & Skinner, H. B. (2001). Prediction of fracture location in the proximal femur using finite element models. *Medical Engineering & Physics*, *23*, 657–664.
3. Dragomir-Daescu, D., Op Den Buijs, J., McEligot, S., Dai, Y. F., Entwistle, R. C., Salas, C., et al. (2011). Robust QCT/FEA models of proximal femur stiffness and fracture load during a sideways fall on the hip. *Annals of Biomedical Engineering*, *39*(2), 742–755.
4. Mirzaei, M., Keshavarzian, M., & Naeini, V. (2014). Analysis of strength and failure pattern of human proximal femur using quantitative computed tomography (QCT)-based finite element method. *Bone*, *64*, 108–114.
5. Bessho, M., Ohnishi, I., Matsumoto, T., Ohashi, S., Matsuyama, J., Tobita, K., et al. (2009). Prediction of proximal femur strength using a CT-based nonlinear finite element method: Differences in predicted fracture load and site with changing load and boundary conditions. *Bone*, *45*, 226–231.
6. Koivumäki, J. E. M., Thevenot, J., Pulkkinen, P., Kuhn, V., Link, T. M., Eckstein, F., et al. (2012). CT-based finite element models can be used to estimate experimentally measured failure loads in the proximal femur. *Bone*, *50*, 824–829.
7. Michelson, J. D., Myers, A., Jinnah, R., Cox, Q., & Van Natta, M. (1995). Epidemiology of hip fractures among the elderly: Risk factors for fracture type. *Clinical Orthopaedics and Related Research*, *311*, 129–135.
8. Keyak, J. H., Meagher, J. M., Skinner, H. B., & Mote, C. D., Jr. (1990). Automated three-dimensional finite element modelling of bone: A new method. *Journal of Biomedical Engineering*, *12*, 389–397.
9. Keaveny, T. M., Borchers, R. E., Gibson, L. J., & Hayes, W. C. (1993). Trabecular bone modulus and strength can depend on specimen geometry. *Journal of Biomechanics*, *26*, 991–1000.
10. Les, C. M., Keyak, J. H., Stover, S. M., Taylor, K. T., & Kaneps, A. J. (1994). Estimation of material properties in the equine metacarpus with use of quantitative computed tomography. *Journal of Orthopaedic Research*, *12*, 822–833.
11. Keller, T. S. (1994). Predicting the compressive mechanical behavior of bone. *Journal of Biomechanics*, *27*, 1159–1168.
12. Yosibash, Z., Tal, D., & Trabelsi, N. (2010). Predicting the yield of the proximal femur using high-order finite-element analysis with inhomogeneous orthotropic material properties. *Philosophical Transactions of the Royal Society A: Mathematical, Physical and Engineering Sciences*, *368*, 2707–2723.
13. Keyak, J. H., Rossi, S. A., Jones, K. A., & Skinner, H. B. (1997). Prediction of femoral fracture load using automated finite element modeling. *Journal of Biomechanics*, *31*(2), 125–133.
14. Reilly, D. T., & Burstein, A. H. (1975). The elastic and ultimate properties of compact bone tissue. *Journal of Biomechanics*, *8*, 393–405.
15. Yoshikawa, T., Turner, C. H., Peacock, M., Slemenda, C. W., Weaver, C. M., Teegarden, D., et al. (1994). Geometric structure of the femoral neck measured using dual-energy x-ray absorptiometry. *Journal of Bone and Mineral Research*, *9*(7), 1053–1064.
16. Nishiyama, K. K., Gilchrist, S., Guy, P., Cripton, P., & Boyd, S. K. (2013). Proximal femur bone strength estimated by a computationally fast finite element analysis in a sideways fall configuration. *Journal of Biomechanics*, *46*, 1231–1236.

17. Robinovitch, S. N., Hayes, W. C., & McMahon, T. A. (1991). Prediction of femoral impact forces in falls on the hip. *Journal of Biomechanical Engineering*, *113*, 366–374.
18. Kim, J. S., Park, T. S., Park, S. B., Kim, J. S., Kim, I. Y., & Kim, S. I. (2000). Measurement of femoral neck anteversion in 3D. Part 1: 3D imaging method. *Med. Biol. Eng. Comput.*, *38*, 603–609.
19. Atilla, B., Oznur, A., Caglar, O., Tokgozoglu, M., & Alpaslan, M. (2007). Osteometry of the femora in Turkish individuals: A morphometric study in 114 cadaveric femora as an anatomic basis of femoral component design. *Acta Orthop. Traumatol. Turc.*, *41*, 64–68.
20. Sariali, E., Mouttet, A., Pasquier, G., & Durante, E. (2009). Three-dimensional hip anatomy in osteoarthritis: Analysis of the femoral offset. *Journal of Arthroplasty*, *24*, 990–997.
21. Kheirollahi, H., & Luo, Y. (2015). Assessment of hip fracture risk using cross-section strain energy by QCT-based finite element modeling. *BioMed Research International*, *2015*, Article ID 413839.
22. Kheirollahi, H., & Luo, Y. (2015). Identification of high stress and strain regions in proximal femur during single-leg stance and sideways fall using QCT-based finite element model. *International Journal of Medical, Health, Biomedical, Bioengineering and Pharmaceutical Engineering*, *9*(8), 541–548.
23. Nikander, R., Kannus, P., Dastidar, P., Hannula, M., Harrison, L., Cervinka, T., et al. (2009). Targeted exercises against hip fragility. *Osteoporosis International*, *20*, 1321–1328.
24. Abrahamsen, B., van Staa, T., Ariely, R., Olson, M., & Cooper, C. (2009). Excess mortality following hip fracture: A systematic epidemiological review. *Osteoporosis International*, *20*, 1633–1650.
25. Wolff, J. (1986). *The law of bone remodeling (translation of the German 1892 edition)*. Berlin: Springer.
26. Frost, H. M. (1994). Wolff's law and bone's structural adaptations to mechanical usage: An overview for clinicians. *The Angle Orthodontist*, *64*, 175–188.
27. Røhl, L., Larsen, E., Linde, F., Odgaard, A., & Jørgensen, J. (1991). Tensile and compressive properties of cancellous bone. *Journal of Biomechanics*, *24*, 1143–1149.
28. Bayraktar, H. H., Morgan, E. F., Niebur, G. L., Morris, G. E., Wong, E. K., & Keaveny, T. M. (2004). Comparison of the elastic and yield properties of human femoral trabecular and cortical bone tissue. *Journal of Biomechanics*, *37*, 27–35.
29. de Bakker, P. M., Manske, S. L., Ebacher, V., Oxland, T. R., Crompton, P. A., & Guy, P. (2009). During sideways falls proximal femur fractures initiate in the superolateral cortex: Evidence from high-speed video of simulated fractures. *Journal of Biomechanics*, *42*, 1917–1925.